Journal Pre-proofs

Low-cost flash graphene from carbon black to reinforce cementitious composites for carbon footprint reduction

Danna Wang, Siqi Ding, Xinyue Wang, Liangsheng Qiu, Hanyao Qin, Yi-Qing Ni, Baoguo Han

PII: S1385-8947(24)08417-1
DOI: https://doi.org/10.1016/j.cej.2024.156926
Reference: CEJ 156926

To appear in: *Chemical Engineering Journal*

Received Date: 4 June 2024
Revised Date: 7 October 2024
Accepted Date: 18 October 2024

Please cite this article as: D. Wang, S. Ding, X. Wang, L. Qiu, H. Qin, Y-Q. Ni, B. Han, Low-cost flash graphene from carbon black to reinforce cementitious composites for carbon footprint reduction, *Chemical Engineering Journal* (2024), doi: https://doi.org/10.1016/j.cej.2024.156926

Low-cost Flash Graphene from Carbon Black to Reinforce Cementitious Composites for Carbon Footprint Reduction

Danna Wang[1], Siqi Ding[2, *], Xinyue Wang[1], Liangsheng Qiu[1], Hanyao Qin[1], Yi-Qing Ni[2], Baoguo Han[1, *]

[1] *School of Civil Engineering, Dalian University of Technology, Dalian, 116024 China*

[2] *Department of Civil and Environmental Engineering, The Hong Kong Polytechnic University, Hung Hom, Kowloon, Hong Kong Special Administrative Region of China*

** Corresponding author: s.q.ding@connect.polyu.hk, hithanbaoguo@163.com*

Abstract

With the merits of high quality, cost-effectiveness, and high yield efficiency, flash Joule heating (FJH) emerges as an efficient means for mass production of flash graphene (FG). It creates prerequisites for the large-scale application of graphene in reinforcing cementitious composites, thus opening innovative possibilities for curbing carbon emissions and fostering the sustainable evolution of cementitious composites. In this study, two types of FGs, including high-purity FG (FG-G) and conductive FG (FG-D), are successfully synthesized via FJH process using carbon black as the carbon source. FG-G features a low I_D/I_G of 0.52, and exhibits higher graphitization and structural orderliness with fewer defects compared to the FG-D. The addition of 0.25 wt.% FG-D increases the compressive strength, flexural strength, and flexural ultimate strain of cementitious composites by 16.48 MPa/16.8%, 1.43 MPa/37.2%, and nearly 2600 με/550%, respectively. The microstructure characterization results reveal that FG reduces the matrix defects, enhances both the matrix microstructure and calcium silicate hydrate gel nanostructure, which is advantageous for matrix refinement, inhibition of microcrack aggregation and propagation, and load transfer efficiency. Its disorderly stacked turbine structure also contributes to robust interface bonding and friction with cement matrix, thus facilitating the strengthening and toughening of cementitious composites. This study introduces a potential avenue to develop widely applicable and versatile cementitious composites with high performance and low CO_2 emission by using small graphene as reinforcement.

Keywords: Flash graphene; Synthesis; Cementitious composites; Properties; Microstructure

1. Introduction

Graphene with superior mechanical, thermal and electrical properties [1, 2], is regarded as a revolutionary material for the future, and has gained significant attention

across diverse fields such as materials science [3], energy [4], biomedicine [5], etc. It has excellent strength and toughness, with a theoretical Young's modulus of up to 1.0 TPa, an inherent tensile strength of 130 GPa [6], a thermal conductivity of 5300 W/mK [7], a room-temperature carrier mobility of approximately 15000 $cm^2/(V \cdot s)$ [8], and a theoretical specific surface area of 2630 m^2/g. Because of its favorable compatibility with cementitious composites, graphene also holds significant promise in the field of civil engineering materials. As a potential reinforcement, graphene offers novel solutions to address the brittleness and low stability of traditional cementitious composites, particularly in complex and extreme service environments [9-13].

Some studies have explored adding graphene as a modifying nanomaterial into cementitious composites to tailor their mechanical, durability, and functional properties [14, 15]. Gong et al. [16] found that graphene oxide (GO) improved the hydration degree and reduced porosity of cement pastes, thereby enhancing the compressive and tensile strength of 0.03 wt.% GO reinforced cement pastes by 46% and 50%. Han et al. [17] identified that multi-layer graphene (MLG) as an effective nanofiller, could form a widely distributed network in cement matrix and exhibit self-curing ability through water absorption and release of MLG. The maximum increase of 54% in compressive strength and 21% in flexural strength of cementitious composites could be achieved by incorporating 2 vol.% and 1 vol.% MLG, respectively. According to the research of Dong et al. [18], the filling and nucleation effects of graphene improved the micro/nano structure of cementitious composites, i.e., reducing matrix porosity, inhibiting cracks extension through bridging and pulling out effects, and increasing the polymerization degree of calcium silicate hydrate (C-S-H) gels. A maximum increase of 44% in compressive strength, 39% in flexural strength, and 30% in flexural modulus of cementitious composites was achieved by the modification of graphene. In addition, Hong et al. [19] concluded that incorporating a small amount of GO into lightweight high-performance concrete improved its workability and increased its compressive strength, split tensile strength, elasticity modulus, and flexural strength by 24%, 17%, 15%, and 20%, respectively. Rezakhani et al. [20] found that doping 0.1 wt.% GO not only increased the compressive strength of concrete with 50 wt.% ground granulated blast furnace slag (GGBFS) by 40% and flexural strength by 60%, but also reduced its chloride permeability by 70%. This indicated the clear benefits of introducing GO for improving the durability and corrosion performance of GGBFS concrete. Additionally, Sun et al. [21] revealed that cementitious composites filled with MLG exhibited a good electrical property and a sensitive piezoresistive effect, as well as desirable electromagnetic shielding/absorption capabilities, which were about 1.6 times/7 times more than the plain cementitious composite. Dimov et al. [22] also demonstrated that the electrical and thermal properties of graphene modified concrete were improved, and surprisingly, its water permeability was reduced by nearly 400% compared to ordinary concrete.

The modification effects of graphene on cementitious composites are closely linked to its inherent quality and performance. The incorporation of high-quality graphene can also reduce the amount of cement without compromising the properties of cementitious composites, thereby contributing to a decrease in carbon emissions. It has been reported that the doping of 0.03 wt.% graphene in cementitious composites results in a substantial 25–33% reduction in carbon footprint [22-24]. However, the complex and costly process of preparing high-quality graphene poses challenges for the large-scale fabrication of graphene reinforced cementitious composites. Economically,

environmentally friendly and efficient preparation of high-quality graphene stands as a pivotal issue in current research. The commonly used methods for graphene production can be divided into top-down and bottom-up approaches [25, 26]. Top-down approaches such as mechanical exfoliation are commonly employed for large-scale graphene production. However, they often involve extensive solvent consumption and complex treatment processes, which may introduce defects into graphene and lead to quality degradation [27, 28]. While bottom-up methods such as chemical vapor deposition can produce high-quality graphene, their high energy consumption, high cost, and low yield hinder the mass production of graphene [29, 30].

The emergence of flash Joule heating (FJH) method provides an innovative approach for graphene synthesis with high yield and cost-effectiveness. FJH rapidly converts electrical energy into high-density thermal energy (heating to a temperature of 3000 K within 100 milliseconds), thus creating an instantaneous high-temperature and high-pressure local environment that enables the synthesis of graphene within milliseconds [31-33]. In a groundbreaking study in 2020, Luong et al. achieved a gram-scale synthesis of graphene through FJH processing using carbon black (CB) as a carbon source, named flash graphene (FG) [34]. Gram-scale FG can be also produced within a second by FJH using affordable carbon sources like coal, biomass, and CB. Zhu et al. [35, 36] found that biochar with appropriate resistance was self-sufficient to initiate the FJH reaction, thereby exhibiting low carbon emission. Dong et al. [37] used FJH technology to manufacture defective graphene within one millisecond for improving lithium-ion storage capacity. Besides, FG yield of CB and calcined coke can reach 80–90%, with relatively low preparation costs and energy requirements (being only 7.2–9.2 kJ per gram and an electricity cost of about 0.01 CNY) [34, 38]. Moreover, the 2D hexagonal lattices of FG with a turbine structure are stacked in a rotating disordered manner, which can reduce van der Waals force and foster their homogeneous and stable dispersion within solution [31, 32, 39] and strong bonding with cementitious composites. Consequently, the employment of FG into cementitious composites can facilitate the upcycling of CB from industrial waste, enhance the performance of cementitious composites, and reduce the carbon footprint, thus promoting sustainable development of building materials.

In this study, two types of FGs, including high-purity FG (FG-G) and conductive FG (FG-D), were produced using FJH with CB as the carbon source. The mechanical properties of FG reinforced cement pastes were then investigated, as well as the underlying reinforcement mechanism of FG through analyzing the microstructure of the composites. The electrical property and electrical microstructure of FG reinforced cement pastes was also studied and analyzed through alternating current electrochemical impedance spectroscopy (AC-EIS).

2. Materials and methods

2.1 Materials

CB served as the carbon source for FG synthesis, and boric acid was also used for the synthesis of FG-D. Ordinary Portland cement (P·O 42.5R), fly ash, silica fume as well as superplasticizer were employed to fabricate FG reinforced cement pastes. The P·O 42.5R cement were provided by Dalian Onoda Cement Co., Ltd. Their chemical composition and mineral composition of cement clinker are shown in Table 1. Fly ash (grade I) and silica fume (920D type) were respectively produced by Dalian Huaneng

Power Plant and Shanghai Elkem International Trade Co., Ltd. in China. The SiO_2 content, average particle size, bulk density, density and specific surface area of silica fume used in the experiment are 94.2%, 150 nm, 372 kg/m^3, 2.2–2.3 g/cm^3 and 15–30 m^2/g, respectively. Besides, the study adopted 3310E type polycarboxylate acid superplasticizer with a water reduction efficiency of about 30% and a solid content of approximately 45%.

Table 1. Chemical composition and mineral composition of P·O 42.5R cement

Chemical composition (%)	SiO_2	Al_2O_3	Fe_2O_3	CaO	MgO	SO_3	Na_2O
	21.45	5.24	2.89	61.13	2.08	2.05	0.77
Mineral composition (%)	C_3S		C_2S		C_3A		C_4AF
	46.62		26.32		8.99		8.78

2.2 Synthesis and preparation process

2.2.1 Synthesis of FG

FG-G/FG-D were synthesized by FJH reactor (Saine, FJH-2023A) using CB/CB-boric acid as precursors, respectively. The FJH system and their synthesis process are illustrated in Figs. 1(a)–(c). FJH reactor comprises a control module, a vacuum reaction module and a data acquisition module, as illustrated in Fig. 1(a). It has a capacitance capacity of 90 mF and a voltage range of 0–300 V. The preparation process of FG-G is outlined as follows: 1) Weighed 0.1 g of CB and placed it inside a quartz tube (with a length of 70 mm and an inner diameter of 8 mm). 2) Installed graphite plugs at both ends of the quartz tube to form a relatively closed reaction environment. 3) Placed two reaction racks at both ends of the quartz tube, and slightly compressed the CB with electrodes to maintain a resistance of 1 Ω, as shown in Fig. 1(d). 4) Vacuumed the chamber to -0.09 MPa and set the voltage to 190 V for FJH processing. The high-voltage discharge of the capacitor elevated the temperature of CB to 3000 K under 100 ms (The temperature was measured by an infrared temperature probe 1 cm away from the quartz tube). This high energy input and rapid cooling effectively graphitized and converted the amorphous carbon into turbine FG [40]. Figs. 1(e) and (f) depict the flash moment during and after the FJH process, respectively. 5) After the FJH process, the newly formed FG could be used by simply grinding with a mortar.

Besides, the only difference in the preparation of FG-D compared to FG-G is that boric acid mixed with CB was used as the precursor. The doping of boron atoms can alter the local structure and electronic state of graphene, thereby tailoring the electrical properties of FG [41].

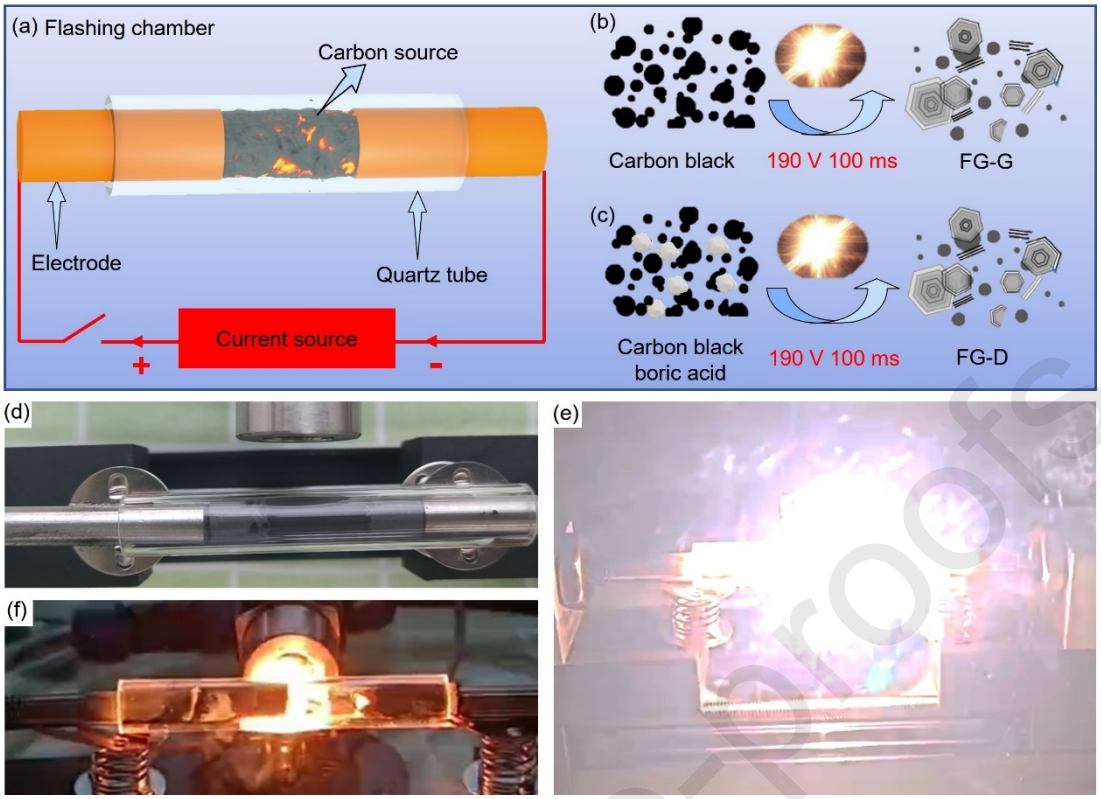

Fig. 1 Synthesis of FG. (a) Schematic diagram of FJH device. Synthesis process of (b) FG-G and (c) FG-D.(d) Precursors and quartz tube before FJH. (e) Flash during FJH process. (f) Sample after FJH.

2.2.2 Preparation of FG reinforced cement pastes

The specific mixing ratios of the FG reinforced cement pastes are detailed in Table 2. Fly ash (Grade I) was introduced to replace 20% of cement to adjust the workability of the cement pastes. The water-cement ratio was maintained at 0.375. Besides, FG-G /FG-D's dosages were 0.25% (0.12 vol.%) and 0.50% (0.24 vol.%) of the cement weight. In Table 2, R0 represents the control group without FG, while R-G0.25/R-D0.25 and R-G0.50/R-D0.50 refer to cement pastes doped with 0.25 wt.% and 0.50 wt.% FG-G/FG-D, respectively.

Table 2. Mixing ratios of FG reinforced cement pastes

Specimen code	Cement	Fly ash	Silica fume	Water	Superplasticizer	FG-G	FG-D
R0	0.8	0.2	0.25	0.3	0.012	–	–
R-G0.25	0.8	0.2	0.25	0.3	0.012	0.002	–

R-G0.50	0.8	0.2	0.25	0.3	0.012	0.004 –
R-D0.25	0.8	0.2	0.25	0.3	0.012	– 0.002
R-D0.50	0.8	0.2	0.25	0.3	0.012	– 0.004

The fabrication of FG reinforced cement paste specimens is as follows: 1) A mixture of water, superplasticizer, and FG was first sonicated for 5 min (400 W, 20 kHz), and followed by cooling to room temperature. 2) Added silica fume to the mixture and stirred at a speed of 1000 ± 100 r/min until achieving uniformity. 3) Half of the cement and fly ash were introduced, and mixed evenly at 1000 ± 100 r/min. The remaining portions of cement and fly ash were then added, and thoroughly stirred. 4) To ensure uniform mixing, the slurry was further stirred at a speed of 2000 ± 100 r/min for 1 min. 5) The mixed cement slurry was poured into different molds (20 mm × 20 mm × 40 mm and 20 mm × 20 mm × 80 mm) and vibrated for 20 s. Copper electrodes were inserted at each end of the former specimen, positioned 1 cm away from the end face for electrical property testing. 6) The specimens were demolded after 24 h and finally cured in a standard chamber at 20 ± 1℃ and 95% relative humidity for a period of 27 days.

2.3 Characterization

2.3.1 Characterization of FG

The morphologies of FG and CB were characterized using field emission scanning electron microscopy (SEM, Nova Nano SEM 450, USA) and field emission transmission electron microscopy (TEM, Tecnai F30, USA). The particle size distribution of FG was measured using a laser particle size meter (LitersizerTM 500, USA). A Brunauer-Emmett-Teller (BET, TriStar II 3020, USA) with N_2 adsorption measurements at 77.3 K was employed to obtain their specific surface area (SSA). The crystalline structures of FG and CB were analyzed using an X-ray diffractometer (XRD, Miniflex 600, Japan) with measurement angles ranging from 5° to 80° at an interval of 0.05°. Meanwhile, a laser confocal micro-Raman spectrometer (inVia Qontor, UK) with a 532 nm laser was applied to identify the characteristic peaks of FG and CB. Spectra were collected over a range of 500 to 3000 cm^{-1}, of which the resolution was 2 cm^{-1}. X-ray photoelectron spectroscopy (XPS, Axis Supra+, UK) analysis was also performed. The measured full spectra had a measurement step size of 1 eV and 160 eV energy flux, while the elemental fine spectra had a measurement step size of 0.1 eV and 40 eV energy flux. All spectra were calibrated against the C 1 s peak (284.8 eV).

2.3.2 Characterization of FG reinforced cement pastes

Compressive test was carried out on 20 mm × 20 mm × 40 mm specimens using a universal testing machine (UTM-100, Australia), and the loading rate was 1.2 mm/min. Simultaneously, two longitudinal strain gauges (BX120-10AA) and transverse strain gauges (BX120-5AA) were affixed to the specimen's side, and the longitudinal and

transverse strain values during the loading process were collected through a dynamic strain indicator (DC-204R, Japan). Moreover, the Young's modulus of cement pastes was derived by assessing the ratio of the stress in the compression direction to the longitudinal strain. The Poisson's ratio of the specimens was obtained by the ratio of the absolute value of transverse strain to longitudinal strain. Besides, specimens measuring 20 mm × 20 mm × 80 mm were employed for flexural test relying on an Instron mechanical testing machine (Instron 5567A, USA). The distance between the two base supports in the flexural test was 60 mm and the loading rate was 0.02 mm/min. A strain gauge (BX120-20AA) was also installed at the bottom span of the specimens to record the mid span tensile strain of the specimen during the flexural process. Both the compressive and flexural strengths of the specimens were averaged over three replicates. Electrochemical measurements were conducted using specimens with dimensions of 20 mm × 20 mm × 40 mm via an Autolab electrochemical workstation (PGSTAT302N, Switzerland). The AC-EIS data collection frequency range for cement pastes was 10^{-2}–10^{6} Hz, and the low amplitude was 10 mV.

The samples for SEM and mercury intrusion porosimetry (MIP) testing were about 5 mm × 5 mm × 5 mm in size, and they were soaked in ethanol for 1 days and then vacuum dried for 2 days before testing. The microstructure of the specimens was observed by SEM, and using energy dispersive X-ray spectroscopy (EDX) tested the Ca/Si ratio of C-S-H gels. MIP measurement was conducted through a mercury porosimeter (Micromeritics AutoPore IV 9600, USA), to analyze cement pastes' porosity as well as pore structure. Besides, sample powders were prepared and passed through an 80-μm sieve, then subjected to various analyses including thermogravimetric analysis (TGA), XRD, Fourier transform infrared spectroscopy (FTIR), and ^{29}Si nuclear magnetic resonance (NMR) tests. TGA testing was performed using a thermal analyzer (TGA8000-Frontier-Clarus SQ8T, USA). The heating range was from room temperature to 1000°C at a rate of 10°C/min under N_2. XRD patterns covering a range from 10° to 70°, were utilized to analyze the hydration products. FTIR analysis was conducted by a spectrometer (EQUINOX55, Germany) to obtain vibrational characteristics of functional groups in hydration products. The wavenumber range was from 400 cm^{-1} to 4000 cm^{-1} with 2.0 cm^{-1} resolution. ^{29}Si NMR test was carried out using a solid-state high power NMR spectrometer (Agilent DD2-500MHz, USA), allowed for the study on silica-oxygen tetrahedron structure of C-S-H gels. Its probe diameter, rotational speed, relaxation time and resonance frequency were 6 mm, 4 kHz, 4 s and 99.29 MHz, respectively. Subsequently, the ^{29}Si NMR spectra of cement pastes were deconvoluted and iteratively fitted by Peakfit software, enabling the calculation of polymerization degree (PD), mean molecular chain length (MCL), and hydration degree (HD) through the provided Eqs. (1) – (3).

$$PD = Q^2 / Q^1 \quad (1)$$

$$MCL = 2(Q^1 + Q^2) / Q^1 \quad (2)$$

$$HD = (Q^1 + Q^2) / (Q^0 + Q^1 + Q^2) \quad (3)$$

where Q^n (n=0, 1, 2, 3, 4) signifies the chemical environment in which silicon (Si) is

situated, and *n* represents oxygen atoms' count shared between silicon-oxygen tetrahedron with its neighboring tetrahedron.

3. Results and discussion

3.1 Morphology and structure of FG

Fig. 2 demonstrates the morphology and structure of the raw CB, the synthesized FG-G and FG-D in this study. TEM images in Fig. 2(b) reveals a typical layered turbine structure of FG. The layer number of FG-G and FG-D is around 10, with a thickness between 3–5 nm. The particle size distribution of FG-G is between 0.5 μm and 1.2 μm, and that of FG-D ranges from 0.4 μm to 1.1 μm (Fig. 2(a), inset). From TEM-EDX mapping results, FG-G only contains carbon, while FG-D contains 7–8% boron with uniform distribution (Fig. 2(c)). Besides, the SSAs of FG-G and FG-D are 108.12 m^2/g and 134.45 m^2/g, respectively. It appears from Fig. 2(d) that FG-D exhibits a smaller particle size and larger SSA compared to FG-G. The XRD spectra for both FG-G and FG-D in Fig. 2(e) show the distinct characteristic peaks at 2θ of 26° and 43°, corresponding to the C(002) and C(100) crystal planes of graphite, respectively [42]. In addition, the Raman spectra in Fig. 2(f) reveal evident D, G, G' bands at 1340 cm^{-1}, 1570 cm^{-1} and 2675 cm^{-1}, respectively. These bands are typical of graphite-based materials. D band represents disordered carbon atoms, while G band indicates the structural orderliness associated with in-plane stretching vibration of sp^2 bonding carbon atoms. G' band is a characteristic peak observed during graphite pyrolysis [43, 44]. Both FG-G and FG-D present appreciable characteristic peaks of graphene as evidenced by XRD and Raman spectroscopy, confirming the successful synthesis of FG using CB as a carbon source through the FJH method.

The intensity ratio I_D/I_G between D and G bands denotes a key indicator of the graphitization degree and structural quality of graphene [45]. As presented in Fig. 2(f), the I_D/I_G values of FG-G and FG-D are 0.52 and 0.96, respectively. Additionally, FG-G shows a more pronounced and broader G-band than FG-D, indicating higher graphitization and structural orderliness with fewer defects in FG-G. The larger I_D/I_G value of FG-D suggests the presence of many substitution defect sites caused by boron doping, as well. The XPS results in Fig. 2(g) also illustrates the presence of doped boron elements in the FG-D sample, whose bonding types are similar to carbon, including graphitic B (BC_3) and boronic B (BCO_2). B_4C is also observed in the B 1s peak of the FG-D sample. The carbon content of FG-G and FG-D is 97.7% and 89.3%, respectively, indicating a higher purity of FG-G. In addition, the doping of boron can improve the conductivity of graphene since boron has one less electron than carbon, creating free "holes" or positive charges in the lattice structure of graphene that can move freely through graphene. This is also revealed by the measured electrical resistivity of FG-G and FG-D via four-probe method, with values of 60–90 mΩ·cm and 20–40 mΩ·cm, respectively.

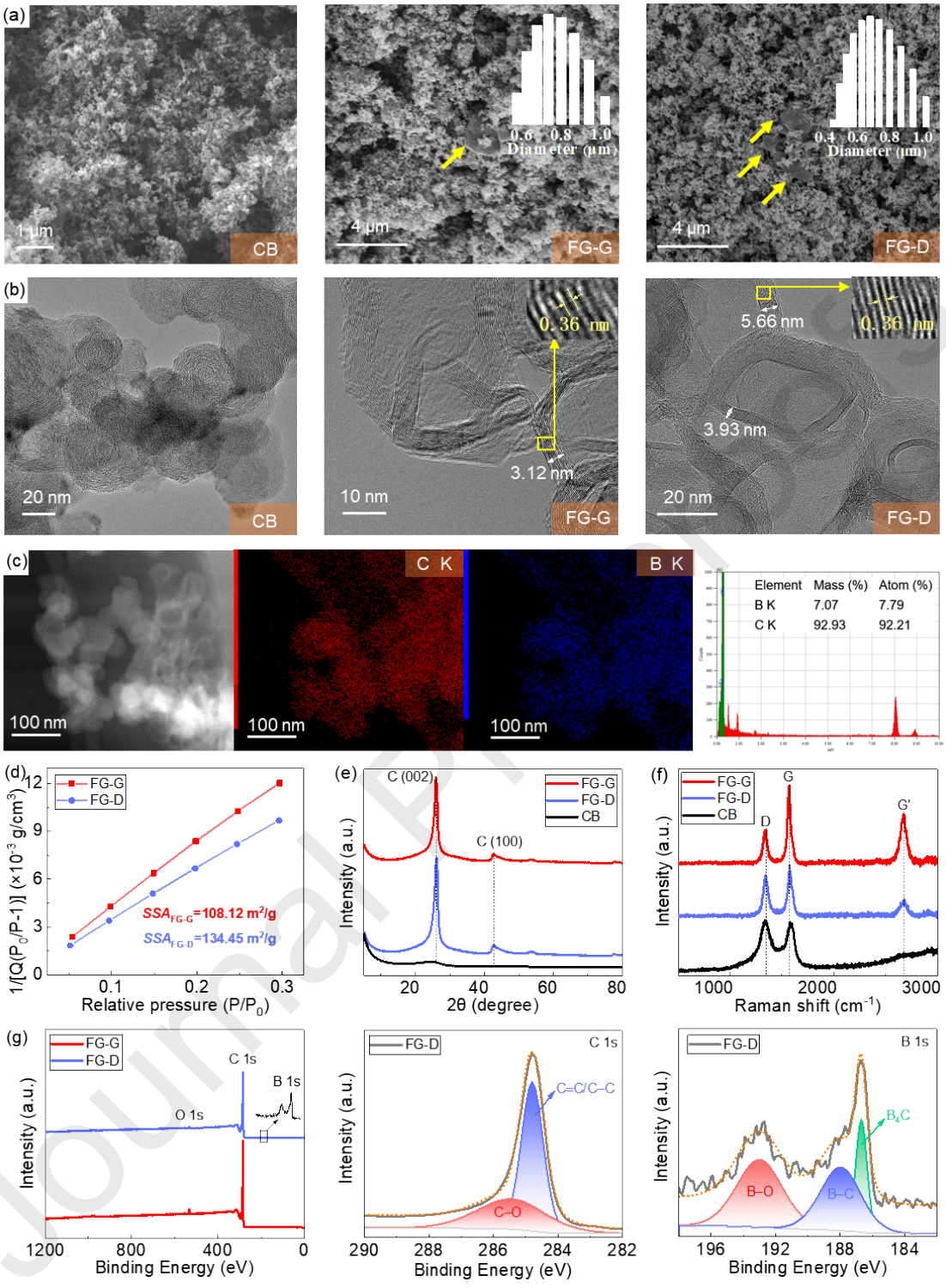

Fig. 2 Morphology and structure characterization of FG and CB. (a) SEM images. Inset shows the particle size distribution. (b) High-resolution TEM images. (c) Element distribution mapping of carbon and boron in FG-D. (d) BET specific surface area of FG-G and FG-D. (e) XRD spectra. (f) Raman spectra. (g) XPS elemental analysis of FG-G and FG-D.

3.2 Properties of FG reinforced cement pastes

3.2.1 Mechanical properties

FG modified cement pastes' mechanical properties are presented in Fig. 3. It can be observed from compressive stress-strain curves (Fig. 3(a)) that doping both FG-G and FG-D in cement pastes increases the peak strain and peak stress. It also alters the slope of the curves during the elastic phase. In other words, FG influences the compressive strength of cementitious composites as well as Young's modulus. From Fig. 3(b), incorporating 0.25 wt.% FG-G and FG-D in cement pastes results in a maximal improvement of compressive strength by 12.05 MPa/12.3% and 16.48 MPa/16.8%, respectively. Whereas, as the dosage of FG increases to 0.50 wt.%, the compressive strength decreases but remains higher than the plain specimen. This phenomenon is associated with the small particle size, high specific surface area along with van der Waals force effect of FG, influencing its dispersion in the matrix and the workability of the matrix, especially at high dosage. Additionally, it is evident from the flexural stress-strain curves in Fig. 3(c) that adding FG notably enhances the yield stress of cement pastes. The nonlinear rise phase of FG reinforced cement pastes is also prolonged, particularly evident in the R-G0.50 and R-D0.25 specimens, exhibiting ductility behaviors. Moreover, FG reinforced cement pastes exhibit gently extended descending curves after reaching the peak stress. Specifically, the R-G0.50, R-D0.25 and R-D0.50 specimens exhibit long platform phases at 50–70% of the peak stress, with an ultimate strain of up to 3000 με, signifying a remarkable increase of about 550% over the plain specimen. As presented in Fig. 3(d), incorporating FG-G and FG-D both enhance their flexural strength obviously. 0.25 wt.% FG-G and FG-D reinforced cement pastes achieves the greatest improvements, with 0.90 MPa/23.3% and 1.43 MPa/37.2%, respectively. Besides, the flexural strength is negatively correlated with FG content, aligning with the variation pattern of compressive strength.

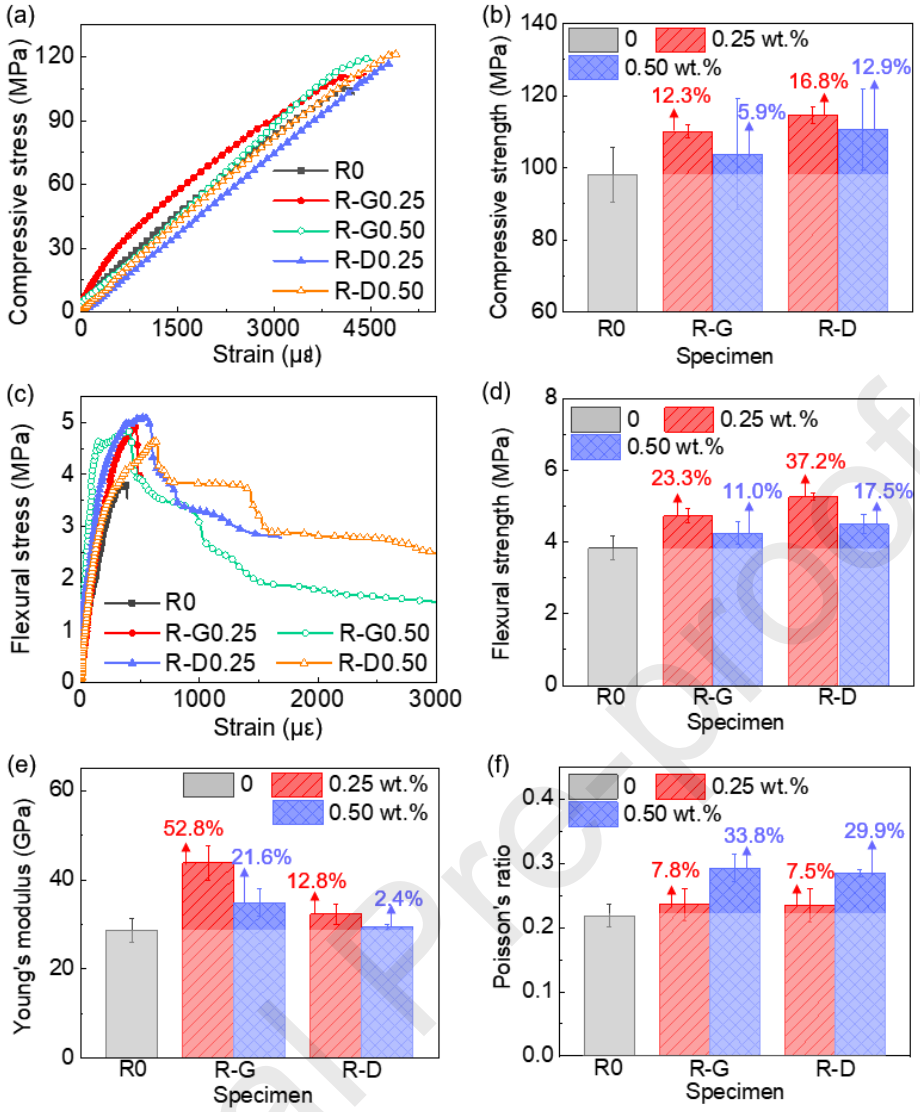

Fig. 3 Mechanical properties of FG reinforced cement pastes. (a) Compressive stress-strain curves. (b) Compressive strength. (c) Flexural stress-strain curves. (d) Flexural strength. (e) Young's modulus. (f) Poisson's ratio.

Figs. 3(e) and (f) demonstrate that the addition of FG significantly improves the Young's modulus and Poisson's ratio of FG reinforced cement pastes. It indicates that FG is conducive to improving the elastic deformation resistance and transverse deformation ability of the composites. Similar to the compressive strength results, cement paste doped with 0.25 wt.% FG shows the greatest enhancement in the Young's modulus. The Young's modulus of R-G0.25 and R-D0.25 specimens can reach 43.80 GPa and 32.33 GPa, respectively, with increase rates of 52.8% and 12.8% compared to the plain specimen. With increasing FG-G and FG-D doping, the Young's modulus of the composites tends to decrease, while the Poisson's ratio increases. Incorporating 0.50 wt.% FG-G/FG-D can achieve improvements of 33.8%/29.9% in Poisson's ratio of cement pastes.

For the two FG nanofillers, FG-D demonstrates a slightly greater effectiveness

than FG-G in improving the mechanical strength of cement pastes. This difference may be attribute to the smaller particle size, larger SSA, and more disordered structure of FG-D compared to FG-G, resulting in a stronger interfacial bond strength with cement matrix. Whereas the Young's modulus improvement of FG-G reinforced cement pastes surpasses that of FG-D. Their enhancement mechanisms are discussed in detail in Section 3.3, by means of microstructural analysis.

3.2.2 Electrical properties

Fig. 4 presents the EIS diagrams of FG reinforced cement pastes at 28 days, obtaining through AC-EIS measurements. As depicted in the Bode plots (Figs. 4(a) and (b)), a consistent pattern of decreasing resistance from low to high frequencies is observed. Apparently, neither FG-G nor FG-D substantially increase the electrical properties of composites, especially at the low concentration of 0.25 wt.%. Adding FG results in the electrical impedance of cement pastes at 28 days similar or slightly lower than the plain specimen. Only R-G0.50 exhibits the lowest electrical impedance of 7.74×10^4 Ω and 6.83×10^3 Ω at frequencies of 10^{-2} Hz and 10^6 Hz, respectively, with the reduction of 29.5% and 23.9% compared to the plain specimen. The doping of FG has no appreciable impact on the electrical properties of cementitious composites, probably owing to the low FG dosage. With FG dosage below the percolation threshold, a complete conductive network cannot be formed in the cement matrix.

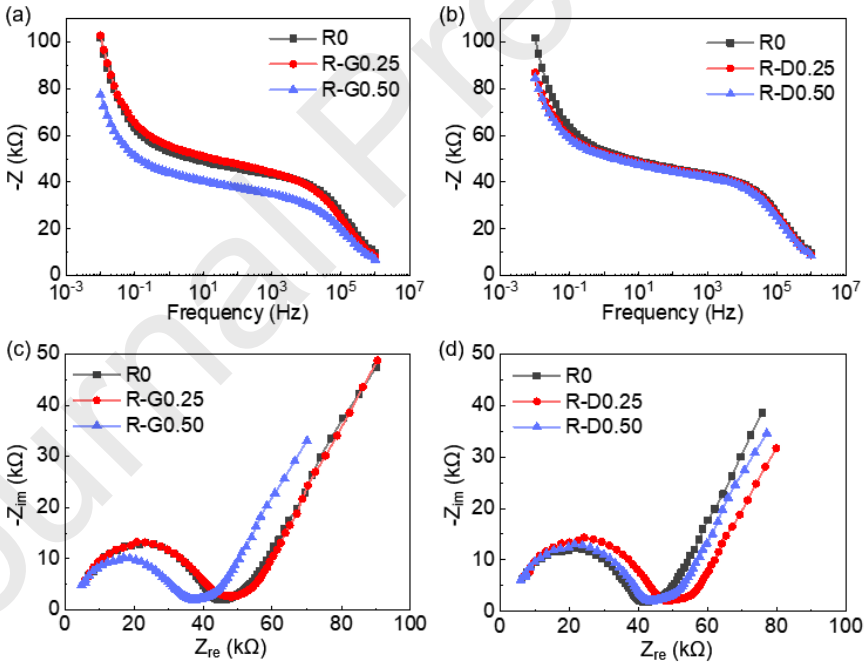

Fig. 4 EIS spectra of cement pastes after curing for 28 days. Bode plots of cement pastes reinforced by (a) FG-G and (b) FG-D. Nyquist plots of cement pastes reinforced by (c) FG-G and (d) FG-D.

Figs. 4(c) and (d) illustrate the Nyquist plots of EIS for cement pastes without and

with FG. The topological characteristics of FG reinforced cement pastes are consistent with the typical Randle topology of cementitious composites, consisting of high-frequency semicircular arcs and low-frequency linear segments. The high-frequency semicircular arcs are associated with the structure of the cement matrix (e.g., hydration products, water content, and ionic concentration) and the conductive components. Meanwhile, the low-frequency linear segments primarily correspond to the charge diffusion in electrochemical reactions involving the stainless-steel electrode, and the resulting impedance is known as Warburg impedance [46]. As presented in Fig. 4(c), the Nyquist plot of R-G0.50 shifts leftward along the real axis compared to the plain cement paste, accompanied by a reduction in the semicircle diameter. It means the impedance of the entire system decreases. This reduction is attributed to the high conductivity of graphene, facilitating a portion of the current to flow directly through the conductive FG filler rather than the less conductive cement matrix. However, due to the low dosage of FG, it still fails to form a complete conductive network in the matrix, resulting in limited improvement in the conductivity of the composites. The linear segment dominated by charge diffusion in EIS at low frequencies also suggests that ion conduction still exerts the predominant function in cement pastes' conductive path [21]. Additionally, the semicircle diameters of the Nyquist curves of cement pastes doped with 0.25 wt.% FG-G/FG-D are both slightly increased, indicating an increase in the impedance of the cement system. This may be associated with the large specific surface area of FG that helps to adsorb free water and reduce ionic mobility [47, 48]. Moreover, FG reinforced cement pastes have a dense pore structure that inhibits ion transport, thereby increasing the material's impedance [47, 49]. In other words, it demonstrates that FG is beneficial for improving the pore structure in matrix and optimizing pore size distribution, as further confirmed in the MIP analyses in Section 3.3.

3.3 Modification mechanisms

The macroscopic performances of cementitious composites are inextricably linked to their matrix microstructure as well as hydration properties. To elucidate the underlying mechanisms of cement pastes modified by FG with favorable mechanical behavior, SEM, EDX, MIP, TGA, XRD, FTIR, and ^{29}Si NMR tests are conducted on 0.25 wt.% FG-G/FG-D reinforced cement pastes.

3.3.1 Microscopic morphology and pore structures

Figs. 5(a) and (b) exhibit the SEM images of fracture surfaces of cement pastes. As demonstrated in Fig. 5(a), the plain cement paste has a large number of directionally distributed large-sized CH crystals, which is detrimental for its mechanical strength development [50, 51]. Doping FG reduces the size of CH crystals, potentially due to the dense matrix of composites with FG limiting the space for CH growth [52], thus inhibiting the initiation and development of cracks. As well, there have fewer defects and denser microstructures in FG reinforced cement pastes, especially in the R-D0.25 sample, compared to the looser microstructure of sample without FG. It is also clearly visible from Fig. 5(b) that there is a substantial amount of low-density C-S-H gels in R0 matrix. The C-S-H gels' structure in cement pastes with FG is more compact, since FG can be served as a nucleation site to generate high-density C-S-H gels along FG sheets. The tough FG-C-S-H composite structure thereby improves the mechanical performances of cement pastes [15, 53]. The SEM images also reflect that FG favors the reduction of the number and size of pores in matrix, therefore quantitative pore

structure analysis was conducted on the sample through MIP.

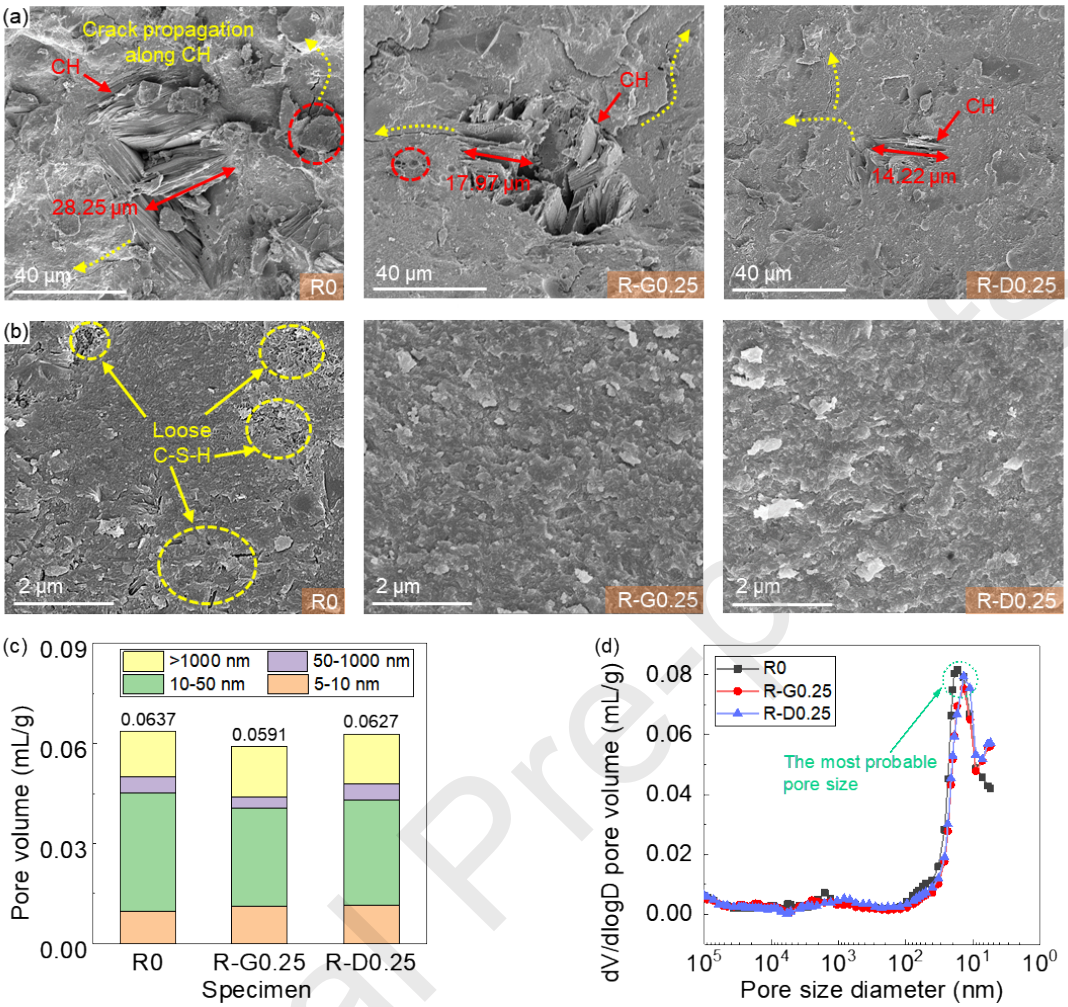

Fig. 5 Microscopic morphology and pore structure of cement pastes filled with FG and without FG. (a) SEM images of matrix microstructure. (b) SEM images of C-S-H gel morphology. (c) Pore volume distribution. (d) Pore size distribution.

Figs. 5(c) and (d) illustrates the pore structure of matrix tested through MIP. Table 3 lists their pore structure characteristic parameters. The introduction of FG marginally reduces the porosity of cement matrix, compared to the plain specimen. Fig. 5(c) plots the volume distribution of four categories of pore structures in cement matrix based on pore size, including gel pores <10 nm existing in C-S-H gels; fine capillary pores of 10–50 nm between external hydration products; 50–1000 nm medium and large capillary pores, mainly formed by free water evaporation and cement hydration shrinkage; large pores greater than 1000 nm originating from the insufficient mixing or vibration [54, 55]. With respect to the R0 sample, R-G0.25 and R-D0.25 samples both show an increase in gel pore volume and a decrease in capillary pore volume, indicating that the doping of FG contributes to the homogenization of pore size distribution in matrix. Furthermore, the most probable pore sizes of both R-G0.25 and R-D0.25 in Fig. 5(d), along with their corresponding mercury intakes are decreased. Their most

probable pore size is 13.73 nm, 19.8% lower than that of the blank group at 17.11 nm. In other words, the doping of FG-G/FG-D is beneficial for refining the pore structure of the matrix [56]. Simultaneously, the characteristic pore sizes, e.g., median pore size of volume/area, average pore size of cement pastes incorporating 0.25 wt.% FG-G/FG-D are all reduced in comparison with the plain specimen, as illustrated in Table 3. Most of the characteristic pore sizes of the plain specimen fall within the fine capillary pore range of 10–50 nm, while the median pore diameters of area are 9.82 nm and 9.98 nm for R-G0.25 and R-D0.25, respectively, belonging to the gel pore range. It indicates that the addition of both FG-G and FG-D significantly decreases the majority of pore sizes inside cement matrix and helps to reduce inter-pore connectivity [57, 58]. In summary, FG-G/FG-D enables the formation of more separated fine pores with a uniform pore size distribution in cement pastes, thereby modifying the pore structure, optimizing the overall structure of the matrix, and then improving the mechanical strengths of composites.

Table 3. Pore structure characteristic parameters of FG reinforced cement pastes by MIP

Specimen code	Porosity (%)	Most probable pore size (nm)	Median pore size of volume (nm)	Median pore size of area (nm)	Average pore size (nm)
R0	11.11	17.11	18.38	10.98	17.35
R-G0.25	10.29	13.73	16.80	9.82	16.36
R-D0.25	10.74	13.73	16.88	9.98	16.45

3.3.2 Hydration products' analysis

The hydration products of FG-G/FG-D reinforced cement pastes at 28 days are analyzed through TGA, XRD and FTIR tests, with the results provided in Fig. 6. The TGA/derivatives of thermogravimetric (DTG) curves in Fig. 6(a)/(b) have four distinct mass loss peaks at around 100–250℃, 400–500℃, 650–800℃, and 850℃. The mass loss peak at 100–250°C originates from chemically bound water dehydration in C-S-H gels and ettringite (AFt). At around 400–500°C and 650–800°C, the mass loss peaks come from the decomposition of CH and calcium carbonate ($CaCO_3$), respectively [59]. The decomposition temperatures of CH and $CaCO_3$ in the DTG curves of FG reinforced cement pastes shift towards lower temperatures. Besides, hydration degree is often empirically characterized by the mass loss of the sample during TGA processes, identifying the weight loss of chemically bound water [60]. The total mass loss of R0, R-G0.25 and R-D0.25 is 18.20%, 18.33% and 19.08%, respectively. It appears that the hydration degree of cement pastes incorporating with FG-G at 28 days is comparable to that of R0, while that with FG-D is slightly larger than the plain specimen. This is evidence of an increase in hydration degree of composites reinforced by FG. It shows that the introduction of FG-D may promote the cement hydration by serving as

adsorption cores for hydration products, water, and ions in cement matrix, resulting in the improved mechanical strength [17, 61, 62].

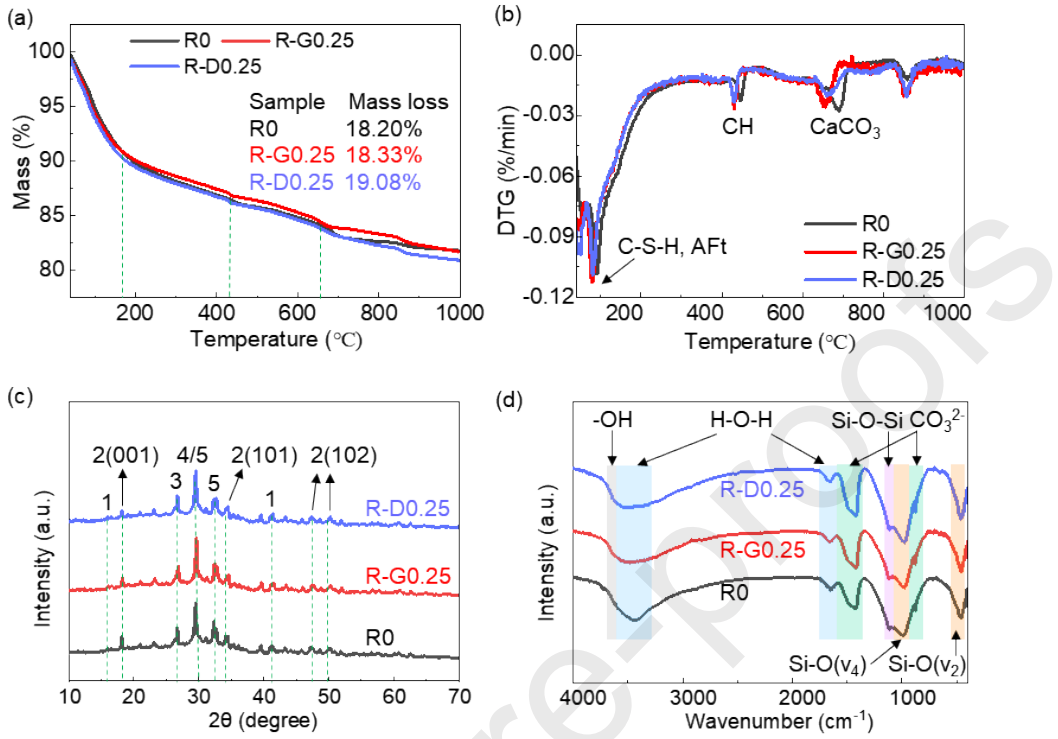

Fig. 6 Hydration products' analysis of FG reinforced cement pastes at 28 days. (a) TGA curves. (b) DTG curves. (c) XRD spectra. (d) FTIR spectra.

Fig. 6(c) presents the XRD spectra of FG reinforced cement pastes. No new diffraction peaks are formed in the XRD spectra of specimens incorporating FG, i.e., FG is not involved in the hydration reaction of the composites. Consistent with the TGA results, the XRD spectra exhibit that the introduction of FG decreases the CH diffraction peak intensity of cement pastes, and the $CaCO_3$ diffraction peak intensity of the R-D0.25 specimen is higher than that of the composite without FG. Furthermore, the peak intensity of C_3S in cement pastes doped with FG is apparently weaker compared to the plain paste without FG, suggesting that the doping of FG promotes the cement hydration and consumes C_3S, consistent with the TGA results.

The FTIR spectra in Fig. 6(d) reveal vibration bands of various functional groups, including -OH, H-O-H, CO_3^{2-}, Si-O-Si, and Si-O groups. The band at 3640 cm^{-1} belongs to -OH stretching vibration band in the hydration product CH. The bands around 3435 cm^{-1} and 1650 cm^{-1} represent the H-O-H stretching vibration and bending vibration of bound water in hydration products, respectively. The CO_3^{2-} asymmetric stretching vibration (1415 cm^{-1}), as well as the CO_3^{2-} out-of-plane bending vibration (875 cm^{-1}) are derived from the carbonate formed after CH carbonation. The 1115 cm^{-1} band represents the Si-O-Si asymmetric stretching vibration from AFt. The 970 cm^{-1} and 455 cm^{-1} bands denote asymmetric stretching vibration (v_4) and in-plane bending vibration

(v_2) of Si-O in silica-oxygen tetrahedron, respectively [63]. The incorporation of FG-G/FG-D does not form new vibration bands or significant change in band positions, further confirming FG-G/FG-D does not involve the hydration reaction of cement pastes.

Fig. 6(d) demonstrates that the -OH vibration bands of CH in R0/R-G0.25/R-D0.25 are all not notable, while the bands of CO_3^{2-} groups are obvious. This suggests that all samples have undergone carbonization, particularly pronounced in R-D0.25, consistent with the TGA and XRD results. Additionally, compared to R0, the Si-O (v_4) and Si-O (v_2) band are deeper and sharper for R-G0.25 and R-D0.25, especially for R-D0.25. As hydration proceeds, the shifts of Si-O (v_4) and Si-O (v_2) move towards higher wave numbers and the vibration bands intensify, indicating the generation and polymerization of the C-S-H phase [52, 63]. Thus, the enhancement of the Si-O (v_4) and Si-O (v_2) band intensity in R-G0.25/R-D0.25 suggests that the doping of FG is beneficial for improving the polymerization degree of C-S-H. Meanwhile, the vibration band of H-O-H group in R-G0.25 and R-D0.25 shifts towards higher wave numbers, with respect to that in R0, indicating a reduce in free water and an enhancement in capillary and gel water. This demonstrates that the incorporation of FG helps to refine pore structure of cement pastes, consistent with MIP analysis results [64].

3.3.3 C-S-H gel structures' analysis

To study the structure of C-S-H gels in FG reinforced cement pastes, the elemental compositions of the cement pastes, particularly regarding the Ca/Si ratios are characterized through EDX analysis results. The average Ca/Si ratios of the control sample, cement pastes doped with 0.25wt.% FG-G and 0.25wt.% FG-D are 1.09, 0.90, and 0.81, respectively. The decreased Ca/Si ratios in C-S-H gels with the addition of FG-G and FG-D suggests its interlayer decalcification resulting in a conversion of the silica-oxygen tetrahedra from dimers to dimer short-chain forms [65, 66]. This transition leads to an increase in the polymerization degree and density of C-S-H gels, thus reinforcing the microstructure of matrix along with its macroscopic properties.

The silicon in C-S-H gels has nuclear magnetic properties, allowing for the quantitative analysis of the nuclear ^{29}Si chemical environment using NMR techniques. Fig. 7 shows the original ^{29}Si NMR spectra and the deconvolution spectra obtained by Gaussian fitting and peak splitting processed through Peakfit software of FG reinforced cement pastes. Table 4 details the results of deconvolution calculations of ^{29}Si NMR spectra of cement pastes. Here, Q^n (n=0, 1, 2, 3, 4) denotes the chemical environment Si situated. Specifically, Q^0 denotes a monomer silicate of unhydrated cement clinker minerals. Q^1 represents a silica-oxygen tetrahedron with one shared oxygen atom, positioned at the end of the C-S-H straight chain, while Q^2 denotes a dimer short chain connected to two silica-oxygen tetrahedron, existing in the middle of the C-S-H straight chain. Q^3 stands for a silica-oxygen tetrahedron sharing three oxygen atoms, generally found in branched networks, sheet or lamellar structures. Q^4 characterizes the silica-oxygen tetrahedron linked to four silica-oxygen tetrahedron to form a highly polymerized three-dimensional spatial network structure, derived from SiO_2 in silica fume and fly ash [67]. The resonance signals Q^0, Q^1, Q^2 Q^3 and Q^4 on spectra are situated within the ranges of -68~-76 ppm, -76~-82 ppm, -82~-88 ppm, -88~-98 ppm and -98~-129 ppm, respectively.

The Q^0 values of R-D0.25 are slightly lower than that of the blank group (Fig. 7, Table 4). This implies a reduction in the content of unhydrated monomer silicate in cement pastes filled with FG. The lower Q^0 value suggests that the incorporation of FG promotes further reaction of unhydrated cement clinker, resulting in increased hydration degree of composites, although its effect is minor from the calculated results in Table 4. While FG-G has no effect on improving cement hydration degree, which is consistent with the TGA results. In addition, the lower Q^1 and higher Q^2 in R-G0.25/R-D0.25 with respect to R0 indicates a condensation of the silica-oxygen tetrahedral structure in C-S-H gels from dimers to dimer short-chain structure. This observation reveals the vital of FG in promoting the transition of silica-oxygen tetrahedron to higher polymerization structures, thereby improving the polymerization degree. Similar results are drawn from FTIR spectra analysis and Ca/Si ratio analysis. The PD/MCL results of C-S-H gels in cement pastes are provided in Table 4, showing that the incorporation of FG-G/FG-D improves the PD from the original 0.65 to 1.53/0.75, an increase of 135.4%/15.4%. Besides, the MCL of cement paste obtains an increase of 52.9% and 5.4%, with the addition of 0.25 wt.% FG-G and FG-D, respectively.

The formation of C-S-H gels' silicate chain structure arises from the dehydration and condensation processes between protonated silicate monomers [68]. The strong adsorption of FG can significantly reduce the Ca^{2+} concentration in C-S-H gels, thus inducing interlayer decalcification of C-S-H gel [68, 69]. Subsequently, both Si-O-Ca and Ca-OH bonds in the silicate structure are disrupted, and the lost Ca^{2+} positions are compensated by H^+, in favor of the formation of protonated Si-OH groups. Thereafter, the dehydration and condensation of Si-OH groups with silica-oxygen tetrahedron elongate the silicate chain length, markedly improving their structural ordering as well as the polymerization degree. Furthermore, graphene with water-absorbing properties decreases the protonated water and shorten the distance of Ca, O, and Si groups in C-S-H gels, thus enhancing the chemical bonds and consequently improving the PD [68].

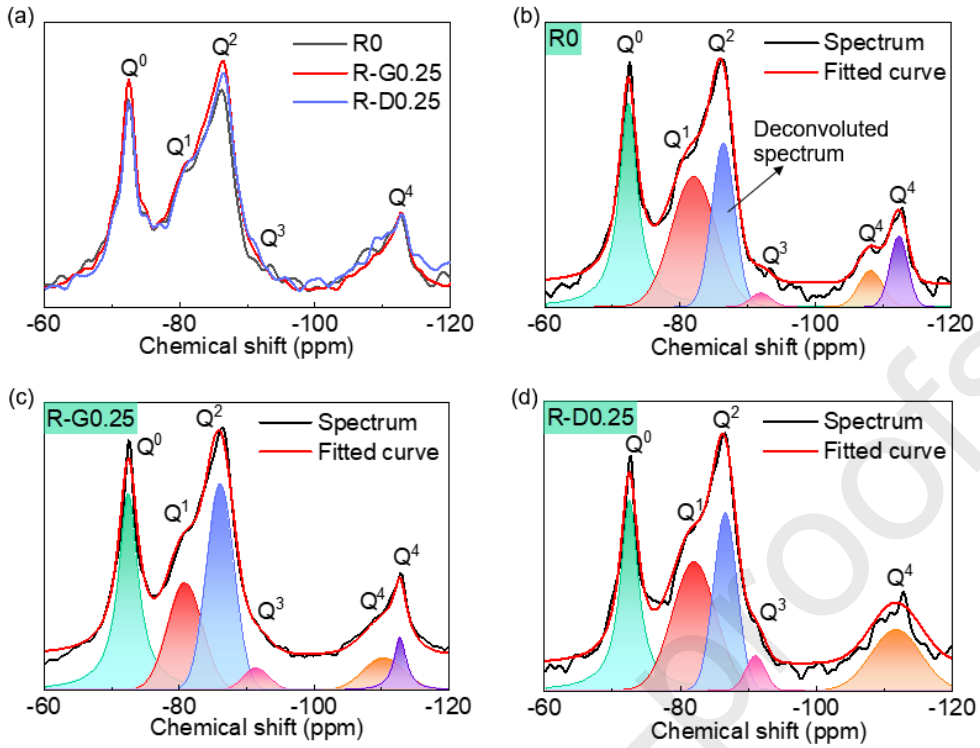

Fig. 7 Original ^{29}Si NMR spectra and deconvoluted ^{29}Si NMR spectra of FG reinforced cement pastes. (a) Original ^{29}Si NMR spectra. Deconvoluted ^{29}Si NMR spectra of (b) R0, (c) R-G0.25 and (d) R-D0.25.

537

538 Table 4. Deconvolution results of ^{29}Si NMR for FG reinforced cement pastes.

Specimen code	Q^0 (%)	Q^1 (%)	Q^2 (%)	Q^3 (%)	Q^4 (%)	*HD* (%)	*PD*	*MCL*
R0	30.8	33.3	21.8	1.7	12.4	64.1	0.65	3.31
R-G0.25	32.1	20.5	31.4	3.2	12.8	61.8	1.53	5.06
R-D0.25	26.6	30.5	22.7	3.7	16.5	66.6	0.75	3.49

539

540 The comprehensive microstructural analysis highlights that FG as a nanofiller,
541 plays a crucial role in reducing matrix defects, enhancing both the matrix microstructure
542 and C-S-H gel nanostructure. FG-G/FG-D does not involve in cement hydration but
543 FG-D slightly improves the hydration degree of composites, demonstrated by an
544 increase total mass loss in TGA and a decrease in the content of unhydrated monomer

silicate Q^0 in ^{29}Si NMR. According to the SEM, MIP and FTIR analyses, the filling effect of FG can also reduce the matrix defects and the porosity, decrease the most probable pore size, median pore size and average pore size thus refining the pore structure, decrease capillary pore volume while increase gel pore volume thus homogenizing pore size distribution. The optimization of pore structure not only improves the microstructure of the matrix, but also restricts the CH's growth space, thereby reducing their size and optimizing their structure, as can be seen from the SEM and XRD results. In addition, the reduction in Ca/Si ratio, increase in Si-O vibration band intensity in FTIR, increase in PD and MCL in ^{29}Si NMR collectively substantiate that FG improves the ordering and polymerization degree of C-S-H gel structure. These enhancements are advantageous for the improvement of matrix compactness, inhibition of microcrack aggregation and propagation, and reinforcement of load transfer efficiency [18, 70, 71]. Simultaneously, owing to its distinctive turbine shape (especially the rotationally disordered FG-D), FG exhibits intrinsic properties such as interlayer slip and structural fracture, coupled with robust bonding capability and friction with the matrix. These attributes contribute to increased energy absorption during the loading process [72], thus effectively enhancing the crack resistance and toughness of cementitious composites [22, 73, 74]. Furthermore, the spatial interlocking mechanism of FG fosters the formation of three-dimensional network enhancement structure in matrix, offering resistance against load deformation and ultimately improving the mechanical strength of composites [70]. The strengthening and toughening of cementitious composites reinforced by FG holds promise for applications in large-span components, enabling reductions in both size and weight.

3.4 Cost Analysis

The addition of 0.25 wt.% FG in cement pastes results in a remarkable increase of 16.8%/37.2% in compressive/flexural strength, respectively. From Paul Mee's formula, concrete strength is basically proportional to that of binder materials. We can roughly estimate that the FG admixture may lead to an approximately 15% increase in concrete strength as well. This is equivalent to elevating the strength of C40 concrete (with a cement dosage of around 360 kg/m^3) to at least that of C45 concrete (with a cement dosage of approximately 390 kg/m^3) without the additional cement consumption. In other words, by adding 0.25 wt.% FG (0.9 kg/m^3) to C40 concrete, it is possible to prepare C45 concrete, thereby reducing cement consumption by about 30 kg/m^3 and decreasing CO_2 emissions by 24–30 kg/m^3, resulting in an 8% reduction in the carbon footprint (According to the International Energy Agency (IEA), the production of one ton of cement emits approximately 0.63 tons of CO_2 on average [73]). The detailed instructions are provided in Table 5. In addition, the cost assessment reveals that the total cost of 1 m^3 C40 commercial concrete in China is about 365 CNY, while C45 is 385 CNY. The total cost of 1 kg FG is only about 11.5 CNY, with the feedstock cost of 9 CNY (considering a CB price of about 8 CNY/kg, assuming a conversion rate of 90%, the rest of 10% is allocated to the costs of consumable items, manpower, and equipment updating etc.), and the electricity cost of 2.5 CNY (energy consumption of only 7.2×10^6–9.2×10^6 J, industrial electricity price of 1 CNY/ kW·h). In that way, the cost of 1 m^3 C45 concrete obtained by adding FG is about 375 CNY, i.e., a saving of 10 CNY compared to the original cost. Moreover, the microstructure modification of cementitious composites by FG also enhances their durability, leading to considerable reductions in maintenance costs throughout the entire life cycle of building structures. Therefore, the economical and efficient preparation of FG through FJH enables the

effective reinforcement of cementitious composites, then reduces cement consumption of concrete as well as associated life cycle costs in concrete, thus contributing to a significant decrease in carbon footprints and enhancing the sustainability of cement concrete composites. This opens up a new territory to develop widely applicable and versatile cementitious composites with high performance and low CO_2 emission by using small graphene as reinforcement, thus addressing the cracking and brittleness of traditional cementitious composites and catering to structural complexity requirements, as well as advancing sustainable development of building materials.

Table 5. Cement usage and cost of concrete

Item name	Compressive strength	Cement usage	FG dosage	Cost
FG	–	–	–	11.5 CNY/ kg
C40 concrete	About 49 MPa	360 kg/m^3	–	365 CNY/ m^3
C45 concrete	About 54 MPa	390 kg/m^3	–	385 CNY/ m^3
C40 concrete + 0.25 wt.% FG	About 55 MPa	360 kg/m^3	0.9 kg/m^3	375 CNY/ m^3

4. Conclusions

This study uses the green, ultrafast, and low-cost FJH method to synthesize two types of FGs, and systematically studies the mechanical and electrical properties of FG reinforced cement pastes. The enhancement mechanism of cement pastes incorporating FG is undertaken subsequently through a series of microanalyses. The economics of its use for the low-cost, large-scale preparation of graphene concrete is also explored. The main conclusions are set out below:

1) The FJH process provides an economical and efficient method for preparing graphene, with the cost for producing 1 kg FG being only 11.5 CNY when using CB as a carbon source. The both as-synthesized FGs have 10 layers and a thickness of 3–5 nm in a turbine shape. Specifically, FG-G (I_D/I_G of 0.52) is highly graphitized and structurally ordered with fewer defects, while FG-D is characterized by small size and large specific surface area.

2) The addition of FG-G and FG-D in cement pastes can significantly enhance their mechanical properties. FG-D's modification effect on cement pastes is slightly better than FG-G, reaching its peak effectiveness at a dosage of 0.25 wt.%. The compressive/flexural strength of cement pastes containing 0.25 wt.% FG-D can be increased by 16.8%/37.2%. Incorporating FG into cement pastes also leads to an increase in Young's modulus (2.4–52.8%) and Poisson's ratio (7.5–33.8%). Of

particular interest is the approximately 550% increase in flexural ultimate strain of FG reinforced cement pastes. However, the addition of FG has no clear effect on enhancing the electrical property of cement pastes.

3) FG obviously modifies the matrix microstructure by improving hydration degree, reducing porosity, optimizing pore structure, and enhancing the orderliness and polymerization degree of C-S-H gels. This enhancement is advantageous for the improvement of matrix compactness, inhibition of microcrack aggregation and propagation, and reinforcement of load transfer efficiency. Its disorderly stacked turbine structure also contributes to robust interface bonding and friction with cement matrix, thus facilitating the strengthening and toughening of cementitious composites.

CRediT authorship contribution statement

Danna Wang: Data curation, Formal analysis, Investigation, Methodology, Validation, Writing – original draft, Writing – review & editing. **Siqi Ding**: Investigation, Methodology, Project administration, Supervision, Writing – original draft, Writing – review & editing. **Xinyue Wang**: Supervision, Writing – review & editing. **Liangsheng Qiu**: Investigation, Methodology. **Hanyao Qin**: Investigation, Methodology. **Yi-Qing Ni**: Conceptualization, Supervision. **Baoguo Han**: Conceptualization, Funding acquisition, Project administration, Supervision, Writing – original draft, Writing – review & editing.

Declaration of competing interest

The authors declare that they have no known competing financial interests or personal relationships that could have appeared to influence the work reported in this paper.

Acknowledgments

The authors thank the funding supported from the National Science Foundation of China (51978127, 52178188, and 52308236), the Natural Science Joint Foundation of Liaoning Province (2023-BSBA-077), the Provincial-Municipal Joint Fund (Youth Fund) of Guangdong Basic and Applied Basic Research Foundation (2023A1515110437), the Major Science and Technology Research Project of the China Building Materials Federation (2023JBGS10-02), a grant from the Research Grants Council of the Hong Kong Special Administrative Region, China (Grant No. T22-502/18-R) and the funding support by the Innovation and Technology Commission of Hong Kong SAR Government to the Hong Kong Branch of National Engineering Research Center on Rail Transit Electrification and Automation (Grant No. K-BBY1).

659

660 **References**

661 [1] Morrow W. K., Pearton S. J., Ren F. Review of graphene as a solid state diffusion
662 barrier. Small, 2016, 12(1): 120-134.

663 [2] Son Y. W., Cohen M. L., Louie S. G. Energy gaps in graphene nanoribbons.
664 Physical Review Letters, 2006, 97(21).

665 [3] Raccichini R., Varzi A., Passerini S., et al. The role of graphene for electrochemical
666 energy storage. Nature Materials, 2015, 14(3): 271-279.

667 [4] Xu C., Xu B., Gu Y., et al. Graphene-based electrodes for electrochemical energy
668 storage. Energy and Environmental Science, 2013, 6(5): 1388-1414.

669 [5] Yang K., Feng L., Shi X., et al. Nano-graphene in biomedicine: theranostic
670 applications. Chemical Society Reviews, 2013, 42(2): 530-547.

671 [6] Lee C., Wei X., Kysar J. W., et al. Measurement of the elastic properties and
672 intrinsic strength of monolayer graphene. Science, 2008, 321(5887): 385-388.

673 [7] Balandin A. A. Thermal properties of graphene and nanostructured carbon materials.
674 Nature Materials, 2011, 10(8): 569-581.

675 [8] Morozov S. V., Novoselov K. S., Katsnelson M. I., et al. Giant intrinsic carrier
676 mobilities in graphene and its bilayer. Physical Review Letters, 2008, 100(1).

677 [9] Wang N., Wang S., Tang L., et al. Improved interfacial bonding strength and
678 reliability of functionalized graphene oxide for cement reinforcement applications.
679 Chemistry-a European Journal, 2020, 26(29): 6561-6568.

680 [10] Zhao L., Guo X., Song L., et al. An intensive review on the role of graphene oxide
681 in cement-based materials. Construction and Building Materials, 2020, 241.

682 [11] Krystek M., Ciesielski A., Samori P. Graphene-based cementitious composites:
683 Toward next-generation construction technologies. Advanced Functional Materials,
684 2021, 31(27).

685 [12] She W., Wu Z., Yang J., et al. Cement-based biomimetic metamaterials. Journal
686 of Building Engineering, 2024, 94: 110050.

687 [13] Wu Z., Pan H., Huang P., et al. Biomimetic mechanical robust cement-resin
688 composites with machine learning-assisted gradient hierarchical structures. Advanced
689 Materials, 2024, 36(35): 2405183.

690 [14] Alateah A. H. Graphene concrete: Recent advances in production methods,
691 performance properties, environmental impact and economic viability. Case Studies in
692 Construction Materials, 2023, 19.

693 [15] Salami B. A., Mukhtar F., Ganiyu S. A., et al. Graphene-based concrete: Synthesis
694 strategies and reinforcement mechanisms in graphene-based cementitious composites

(Part 1). Construction and Building Materials, 2023, 396.

[16] Gong K., Pan Z., Korayem A. H., et al. Reinforcing effects of graphene oxide on portland cement paste. Journal of Materials in Civil Engineering, 2015, 27(2).

[17] Han B., Zheng Q., Sun S., et al. Enhancing mechanisms of multi-layer graphenes to cementitious composites. Composites Part A-Applied Science and Manufacturing, 2017, 101: 143-150.

[18] Dong S., Wang Y., Ashour A., et al. Nano/micro-structures and mechanical properties of ultra-high performance concrete incorporating graphene with different lateral sizes. Composites Part A-Applied Science and Manufacturing, 2020, 137.

[19] Hong X., Lee J. C., Qian B. Mechanical properties and microstructure of high-strength lightweight concrete incorporating graphene oxide. Nanomaterials, 2022, 12(5).

[20] Rezakhani D., Jafari A. H., Hajabassi M. Durability, mechanical properties and rebar corrosion of slag-based cement concrete modified with graphene oxide. Structures, 2023, 49: 678-697.

[21] Sun S., Ding S., Han B., et al. Multi-layer graphene-engineered cementitious composites with multifunctionality/intelligence. Composites Part B-Engineering, 2017, 129: 221-232.

[22] Dimov D., Amit I., Gorrie O., et al. Ultrahigh performance nanoengineered graphene-concrete composites for multifunctional applications. Advanced Functional Materials, 2018, 28(23).

[23] Anwar A., Mohammed B. S., Wahab M. A., et al. Enhanced properties of cementitious composite tailored with graphene oxide nanomaterial - A review. Developments in the Built Environment, 2020, 1.

[24] De Souza F. B., Yao X., Lin J., et al. Effective strategies to realize high-performance graphene-reinforced cement composites. Construction and Building Materials, 2022, 324.

[25] Novoselov K. S., Fal'ko V. I., Colombo L., et al. A roadmap for graphene. Nature, 2012, 490(7419): 192-200.

[26] Carvalho A. F., Kulyk B., Fernandes A. J. S., et al. A review on the applications of graphene in mechanical transduction. Advanced Materials, 2022, 34(8).

[27] Kauling A. P., Seefeldt A. T., Pisoni D. P., et al. The worldwide graphene flake production. Advanced Materials, 2018, 30(44).

[28] Jolly A., Miao D., Daigle M., et al. Emerging bottom-up strategies for the synthesis of graphene nanoribbons and related structures. Angewandte Chemie-International Edition, 2020, 59(12): 4624-4633.

[29] Jiang L., Niu T., Lu X., et al. Low-temperature, bottom-up synthesis of graphene via a radical-coupling reaction. Journal of the American Chemical Society, 2013,

135(24): 9050-9054.

[30] Ren W., Cheng H.-M. The global growth of graphene. Nature Nanotechnology, 2014, 9(10): 726-730.

[31] Wyss K. M., Beckham J. L., Chen W., et al. Converting plastic waste pyrolysis ash into flash graphene. Carbon, 2021, 174: 430-438.

[32] Huang P., Zhu R., Zhang X., et al. Effect of free radicals and electric field on preparation of coal pitch-derived graphene using flash Joule heating. Chemical Engineering Journal, 2022, 450.

[33] Zhu S., Zhang F., Lu H. G., et al. Flash nitrogen-doped graphene for high rate supercapacitors. Acs Materials Letters, 2022.

[34] Luong D. X., Bets K. V., Algozeeb W. A., et al. Gram-scale bottom-up flash graphene synthesis. Nature, 2020, 577(7792): 647-651.

[35] Zhu X. D., Lin L. T., Pang M. Y., et al. Continuous and low-carbon production of biomass flash graphene. Nature Communications, 2024, 15(1).

[36] Jia C., Pang M. Y., Lu Y. D., et al. Graphene environmental footprint greatly reduced when derived from biomass waste via flash Joule heating. One Earth, 2022, 5(12): 1394-1403.

[37] Dong S., Song Y. L., Su M. Y., et al. Flash Joule heating induced highly defective graphene towards ultrahigh lithium ion storage. Chemical Engineering Journal, 2024, 481.

[38] Wyss K. M., Li J. T., Advincula P. A., et al. Upcycling of waste plastic into hybrid carbon nanomaterials. Advanced Materials, 2023, 35(16).

[39] Advincula P. A., Duy Xuan L., Chen W., et al. Flash graphene from rubber waste. Carbon, 2021, 178: 649-656.

[40] Stanford M. G., Bets K. V., Luong D. X., et al. Flash graphene morphologies. Acs Nano, 2020, 14(10): 13691-13699.

[41] Chen W., Ge C., Li J. T., et al. Heteroatom-doped flash graphene. Acs Nano, 2022, 16(5): 6646-6656.

[42] Choi S. H., Lee J.-K., Kang Y. C. Three-dimensional porous graphene-metal oxide composite microspheres: Preparation and application in Li-ion batteries. Nano Research, 2015, 8(5): 1584-1594.

[43] Berciaud S., Ryu S., Brus L. E., et al. Probing the intrinsic properties of exfoliated graphene: raman spectroscopy of free-standing monolayers. Nano Letters, 2009, 9(1): 346-352.

[44] Ding S. Q., Wang X. Y., Qiu L. S., et al. Self-sensing cementitious composites with hierarchical carbon fiber-carbon nanotube composite fillers for crack development monitoring of a maglev girder. Small, 2023, 19(9).

[45] He C. N., Zhao N. Q., Shi C. S., et al. Fabrication of aluminum carbide nanowires by a nano-template reaction. Carbon, 2010, 48(4): 931-938.

[46] Qin H. Y., Ding S. Q., Ashour A., et al. Revolutionizing infrastructure: The evolving landscape of electricity-based multifunctional concrete from concept to practice. Progress in Materials Science, 2024, 145.

[47] Long W.-J., Gu Y.-c., Xing F., et al. Microstructure development and mechanism of hardened cement paste incorporating graphene oxide during carbonation. Cement and Concrete Composites, 2018, 94: 72-84.

[48] Da Silva G. F., Martini S., Moraes J. C. B., et al. AC impedance spectroscopy (AC-IS) analysis to characterize the effect of nanomaterials in cement-based mortars. Construction and Building Materials, 2021, 269.

[49] Dong B., Qiu Q., Gu Z., et al. Characterization of carbonation behavior of fly ash blended cement materials by the electrochemical impedance spectroscopy method. Cement and Concrete Composites, 2016, 65: 118-127.

[50] Ye Q., Zhang Z., Kong D., et al. Influence of nano-SiO_2 addition on properties of hardened cement paste as compared with silica fume. Construction and Building Materials, 2007, 21(3): 539-545.

[51] Ding S. Q., Xiang Y., Ni Y. Q., et al. In-situ synthesizing carbon nanotubes on cement to develop self-sensing cementitious composites for smart high-speed rail infrastructures. Nano Today, 2022, 43.

[52] Li Z., Corr D. J., Han B., et al. Investigating the effect of carbon nanotube on early age hydration of cementitious composites with isothermal calorimetry and Fourier transform infrared spectroscopy. Cement and Concrete Composites, 2020, 107.

[53] Qureshi T. S., Panesar D. K. Impact of graphene oxide and highly reduced graphene oxide on cement based composites. Construction and Building Materials, 2019, 206: 71-83.

[54] Zhao L., Guo X., Liu Y., et al. Hydration kinetics, pore structure, 3D network calcium silicate hydrate, and mechanical behavior of graphene oxide reinforced cement composites. Construction and Building Materials, 2018, 190: 150-163.

[55] Muller A. C. A., Scrivener K. L., Gajewicz A. M., et al. Use of bench-top NMR to measure the density, composition and desorption isotherm of C-S-H in cement paste. Microporous and Mesoporous Materials, 2013, 178: 99-103.

[56] Oltulu M., Sahin R. Pore structure analysis of hardened cement mortars containing silica fume and different nano-powders. Construction and Building Materials, 2014, 53: 658-664.

[57] Wang J., Dong S., Zhou C., et al. Investigating pore structure of nano-engineered concrete with low-field nuclear magnetic resonance. Journal of Materials Science, 2021, 56(1): 243-259.

[58] Wang J., Wang X., Ding S., et al. Micro-nano scale pore structure and fractal

809 dimension of ultra-high performance cementitious composites modified with
810 nanofillers. Cement and Concrete Composites, 2023, 141.

811 [59] Peschard A., Govin A., Grosseau P., et al. Effect of polysaccharides on the
812 hydration of cement paste at early ages. Cement and Concrete Research, 2004, 34(11):
813 2153-2158.

814 [60] Gomez-Zamorano L. Y., Escalante-Garcia J. I. Effect of curing temperature on the
815 nonevaporable water in portland cement blended with geothermal silica waste. Cement
816 and Concrete Composites, 2010, 32(8): 603-610.

817 [61] Han B., Zhang L., Zeng S., et al. Nano-core effect in nano-engineered cementitious
818 composites. Composites Part A-Applied Science and Manufacturing, 2017, 95: 100-
819 109.

820 [62] Cui X., Han B., Zheng Q., et al. Mechanical properties and reinforcing mechanisms
821 of cementitious composites with different types of multiwalled carbon nanotubes.
822 Composites Part A-Applied Science and Manufacturing, 2017, 103: 131-147.

823 [63] Mollah M. Y. A., Yu W. H., Schennach R., et al. A Fourier transform infrared
824 spectroscopic investigation of the early hydration of Portland cement and the influence
825 of sodium lignosulfonate. Cement and Concrete Research, 2000, 30(2): 267-273.

826 [64] Dong S., Wang D., Ashour A., et al. Nickel plated carbon nanotubes reinforcing
827 concrete composites: from nano/micro structures to macro mechanical properties.
828 Composites Part A-Applied Science and Manufacturing, 2021, 141.

829 [65] Beaudoin J. J., Raki L., Alizadeh R. A ^{29}Si MAS NMR study of modified C-S-H
830 nanostructures. Cement and Concrete Composites, 2009, 31(8): 585-590.

831 [66] Schneider J., Cincotto M. A., Panepucci H. ^{29}Si and ^{27}Al high-resolution NMR
832 characterization of calcium silicate hydrate phases in activated blast-furnace slag pastes.
833 Cement and Concrete Research, 2001, 31(7): 993-1001.

834 [67] Porteneuve C., Korb J. P., Petit D., et al. Structure-texture correlation in ultra-high-
835 performance concrete - A nuclear magnetic resonance study. Cement and Concrete
836 Research, 2002, 32(1): 97-101.

837 [68] Wang J., Han B., Li Z., et al. Effect investigation of nanofillers on C-S-H gel
838 structure with Si NMR. Journal of Materials in Civil Engineering, 2019, 31(1).

839 [69] Han B., Zhang L., Ou J. Smart and multifunctional concrete towards sustainable
840 infrastructures. Singapore: Springer, 2017.

841 [70] Lu Z., Hou D., Meng L., et al. Mechanism of cement paste reinforced by graphene
842 oxide/carbon nanotubes composites with enhanced mechanical properties. Rsc
843 Advances, 2015, 5(122): 100598-100605.

844 [71] Konsta-Gdoutos M. S., Danoglidis P. A., Shah S. P. High modulus concrete:
845 Effects of low carbon nanotube and nanofiber additions. Theoretical and Applied
846 Fracture Mechanics, 2019, 103.

[72] Ho V. D., Ng C.-T., Ozbakkaloglu T., et al. Investigating the reinforcing mechanism and optimized dosage of pristine graphene for enhancing mechanical strengths of cementitious composites. Rsc Advances, 2020, 10(70): 42777-42789.

[73] Wang J., Dong S., Yu X., et al. Mechanical properties of graphene-reinforced reactive powder concrete at different strain rates. Journal of Materials Science, 2020, 55(8): 3369-3387.

[74] Chuah S., Pan Z., Sanjayan J. G., et al. Nano reinforced cement and concrete composites and new perspective from graphene oxide. Construction and Building Materials, 2014, 73: 113-124.

[75] https://www.iea.org/reports/co2-emissions-from-fuel-combustion/cement-production

1. Flash graphene (FG) was rapidly produced by flash Joule heating from carbon black.

2. FG with turbine structure enables strong interfacial bonding with cement matrix.

3. FG can modify C-S-H gel nanostructure of cementitious composites.

4. FG improves the compressive/flexural strength of cement pastes by 16.8%/37.2%.

5. It's a new avenue to reinforce cementitious composites with low cost/CO_2 emission.